

# The impact of turbulence and convection on transport in the Southern Ocean

Taimoor Sohail<sup>1,2</sup>, Catherine A. Vreugdenhil<sup>3</sup>, Bishakhdatta Gayen<sup>4</sup>, and  
Andrew McC. Hogg<sup>1,2</sup>

<sup>1</sup>Research School of Earth Sciences, Australian National University, Canberra, ACT 2601, Australia

<sup>2</sup>ARC Centre of Excellence for Climate Extremes, Australian National University, Canberra ACT 2601,  
Australia

<sup>3</sup>Department of Applied Mathematics and Theoretical Physics, University of Cambridge, Cambridge,  
United Kingdom

<sup>4</sup>Department of Mechanical Engineering, University of Melbourne, Melbourne VIC 3010, Australia

## Key Points:

- We analyse zonal and meridional transport in an idealised Southern Ocean model with resolved convection and turbulence.
- Resolving all scales of motion, zonal transport is insensitive to wind stress, indicating eddy saturation.
- Abyssal meridional overturning is greater than upper overturning, enabled by fluctuating flows, and increases with enhanced wind stress.

This article has been accepted for publication and undergone full peer review but has not been through the copyediting, typesetting, pagination and proofreading process which may lead to differences between this version and the Version of Record. Please cite this article as doi:

Corresponding author: T. Sohail, [taimoor.sohail@anu.edu.au](mailto:taimoor.sohail@anu.edu.au)

10.1029/2018JC014883

**Abstract**

Volume transport in the presence of fully-resolved convection and turbulence is investigated in a re-entrant channel model of the Southern Ocean. The response of the meridional overturning and zonal transport to variations in wind and buoyancy forcing is quantified. Our simulations show two overturning cells - a buoyancy-driven lower cell and a wind-driven upper cell. The lower overturning cell is much larger in meridional extent and magnitude than the upper cell. The mean component of the overturning transport is smaller than the fluctuating component in the lower overturning cell, indicating that transport is dominated by eddies and/or turbulent convective flow. In contrast, the upper cell can be primarily described as a mean flow (indicating minimal eddy compensation). Both cells strengthen with increasing winds, with the upper cell being more sensitive to increasing wind intensity than the lower cell. Scaling for the mean upper overturning is also derived, and matches previous theories which predict a linear sensitivity of the upper cell to wind. Zonal transport remains insensitive to increasing wind stress, suggesting that the system is eddy saturated when turbulence and eddies are resolved. These results suggest that fine-scale flows control zonal transport and abyssal meridional overturning in the Southern Ocean, while wind stress drives the upper meridional overturning transport, highlighting the importance of accurately characterising turbulence and convection in large-scale models.

**1 Introduction**

The Southern Ocean is a crucial component of the global Meridional Overturning Circulation (MOC), which is known to modulate a number of key climatological properties including CO<sub>2</sub> outgassing (Toggweiler et al., 2006; Morrison et al., 2015), meridional heat transport (Talley et al., 2003) and nutrient fluxes (Schmittner & Weaver, 2001). On average, the MOC is characterised by downwelling of cold, negatively buoyant waters in high latitudes, and a gradual upwelling of abyssal waters elsewhere (Lumpkin & Speer, 2007; Kuhlbrodt et al., 2007). The MOC consists of two overturning cells - a lower abyssal cell and an upper cell. The deep downwelling limb of the abyssal cell is associated with Antarctic Bottom Water (AABW) that is derived from dense water produced along the continental shelf of Antarctica. The downwelling limb of the upper cell occurs in northern latitudes and is associated with North Atlantic Deep Water (NADW). The upwelling of both cells occurs predominantly in the Southern Ocean and is regulated by the wind and buoyancy gradient over this region (J. Marshall & Speer, 2012; Talley, 2013). There is also a strong zonal eastward transport in the Southern Ocean known as the Antarctic Circumpolar Current (ACC). The meridional overturning and zonal ACC are dynamically linked, and are modulated by surface buoyancy fluxes and zonal westerly wind stress in the Southern Ocean (Johnson & Bryden, 1989; Straub, 1993; Hogg, 2010; Howard et al., 2015).

Observational work has indicated that the zonal wind stress over the Southern Ocean has been strengthening over past decades (Hande et al., 2012). Hence, the sensitivity of the ACC transport and the upper and lower overturning circulation to wind stress has emerged as an important area of research. However, efforts to measure the overturning have been hampered by a scarcity of data in the region and the broad spatial extent of the overturning. Research has instead relied increasingly on high-resolution (often idealised) modelling studies, which have suggested that mesoscale eddies play a leading-order role in setting the Southern Ocean stratification, and consequently the overturning circulation (Henning & Vallis, 2005; Meredith & Hogg, 2006; Morrison & Hogg, 2013; Munday et al., 2013). In addition, models suggest Southern Ocean transport may be highly sensitive to the model resolution, the eddy parameterisation scheme used and the diapycnal mixing in the system (Cai & Baines, 1996; Ito & Marshall, 2008; Viebahn & Eden, 2010; Nikurashin & Vallis, 2011, 2012; Morrison & Hogg, 2013; Hieronymus et al., 2019).

69 In the upper cell, eddy-driven overturning can partially compensate the mean over-  
70 turning transport with increasing wind, known as *eddy compensation*. Eddy compensa-  
71 tion leads to a relatively small change in the resulting overturning circulation in the limit  
72 of increasing wind stress (Wolfe & Cessi, 2010; Farneti et al., 2010; Abernathy et al., 2011;  
73 Morrison & Hogg, 2013; Munday et al., 2013). Note, however, that full eddy compen-  
74 sation is a theoretical limit; modelling work by Henning and Vallis (2005), Abernathy  
75 et al. (2011) and Bishop et al. (2016) found that eddies are only partially compensated  
76 at realistic values of the wind stress. Using a *depth-density* streamfunction (evaluated  
77 based on the vertical velocity and density of fluid parcels), Zika, Sijp, and England (2013)  
78 and Hogg et al. (2017) also observed partial eddy compensation in large-scale ocean mod-  
79 els.

80 The sensitivity of the lower cell to wind stress remains unclear. On the one hand,  
81 idealised modelling by Munday et al. (2013) found that the abyssal cell intensifies with  
82 increasing wind stress, a result also observed in a high-resolution coupled climate model  
83 (Bishop et al., 2016) and some studies utilising the depth-density streamfunction diag-  
84 nostic (Zika, Sijp, & England, 2013). On the other hand, Nikurashin and Vallis (2011)  
85 and Abernathy et al. (2011) found the opposite trend, with AABW strength reducing  
86 with increasing wind stress. This discrepancy may be attributed to differences in sur-  
87 face buoyancy forcing, model configurations and model resolution, leading to a larger un-  
88 certainty in the prediction of overturning transport in the Southern Ocean.

89 The presence of eddies and fine-scale flows also impacts ACC transport, such that  
90 zonal transport is largely insensitive to changing surface winds (a state known as *eddy*  
91 *saturation*) (Meredith & Hogg, 2006). Eddy-resolving re-entrant channel models have  
92 identified conditions approaching eddy saturation in the ACC (Morrison & Hogg, 2013),  
93 with some higher resolution models reaching a fully eddy saturated state (Munday et  
94 al., 2013). The tendency towards eddy saturation is observed through an increase in eddy  
95 activity, quantified by eddy kinetic energy (EKE). As wind stress increases, the EKE in  
96 the Southern Ocean increases (Hogg et al., 2015; Bishop et al., 2016). These eddies ex-  
97 tract the mean available potential energy in the system, directly affecting the stratifi-  
98 cation and inducing interfacial form stress. Interfacial form stress transports momentum  
99 vertically from the source of momentum at the surface to the sink of momentum at the  
100 bottom. The vertical transport of momentum has been proposed to be proportional to  
101 the EKE in the system (D. Marshall et al., 2017). Hence, eddies generated by baroclinic  
102 instability modulate zonal transport through modifying the interfacial form stress in the  
103 system (Ward & Hogg, 2011; Howard et al., 2015). This phenomenon also appears to  
104 be resolution dependent, with stronger EKE observed in finer-resolution models (Morrison  
105 & Hogg, 2013). As model resolution increases and finer-scale eddies are accommodated,  
106 we can expect to obtain a more accurate estimation of the sensitivity of ACC transport  
to wind.

108 Given the demonstrated importance of fine-scale flows (and the mixing driven by  
109 these flows) in modulating meridional and zonal transport in the Southern Ocean, there  
110 is ample motivation to study this system using a fully resolved idealised model. Using  
111 a set of direct numerical simulations (DNS) of an idealised re-entrant channel domain,  
112 we aim to understand the effect of fine-scale convection and turbulence on zonal and merid-  
113 ional transport in the Southern Ocean, expanding upon work by Sohail et al. (2018). DNS  
114 provides a number of key benefits. Absent of any form of turbulence parameterisation  
115 or convective adjustment scheme, the DNS model fully characterises all scales of motion  
116 (Scotti & White, 2011; Gayen et al., 2014; Barkan et al., 2015; Vreugdenhil et al., 2016).  
117 This allows us to investigate the impact of turbulence and convection on the strength  
118 of the meridional overturning and zonal transport. In addition, the sensitivity of the over-  
119 turning and zonal transport to increasing winds with the presence of turbulence may be  
120 quantified for the first time. Where possible, established scaling relationships between  
121 overturning and wind can also be tested, highlighting how well current large-scale mod-

122 els are parameterising small-scale flows. The problem set-up, numerical details and de-  
 123 scription of governing parameters are outlined in Section 2. The resulting overturning  
 124 circulation and zonal transport in Section 3 sheds light on the impact fine-scale flow fea-  
 125 tures may have on controlling Southern Ocean circulation. Further discussion and con-  
 126 clusions are in Section 4.

## 27 2 Methods

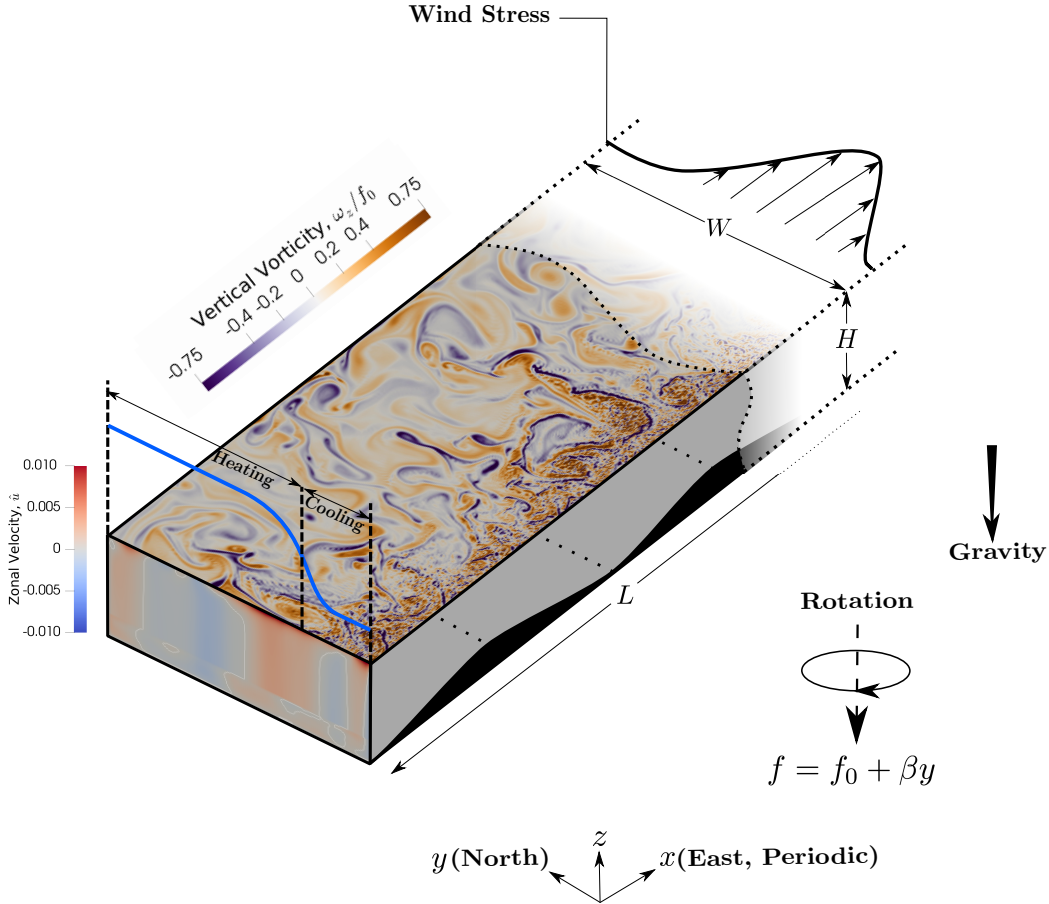


**Figure 1.** An overview of the model domain, with thermally equilibrated flow solutions, for  $S = 2 \times 10^{-4}$ ,  $Ra = 1 \times 10^{12}$  and  $Ro = 0.12$ . *Blue line*: Imposed surface temperature; *black line*: prescribed wind stress. The top surface shows an instantaneous snapshot of the non-dimensionalised vertical component of relative vorticity,  $\hat{\omega}_z = \omega_z / f_0 = f_0^{-1} \nabla \times (u, v)$ , at  $z/H = 0.991$  (within the thermal boundary layer). The meridional plane shows the non-dimensionalised, time-averaged zonal velocity. The overlaid contour line (in white) indicates values of  $\hat{u} = 0$ . Note that the schematic has been truncated in the zonal direction.

28 We employ a DNS of an idealised re-entrant channel with dimensions  $L \times W \times$   
 129  $H$ , corresponding to the  $x$  (east),  $y$  (north), and  $z$  (upward) directions respectively (fig-  
 130 ure 1), similar to that in Sohail et al. (2018). Wind stress and buoyancy forcing are ap-  
 131 plied at the top surface of the model domain. A steady wind stress is imposed in the zonal  
 132 direction ( $x$ ) with a sinusoidal variation in the meridional ( $y$ ) direction which has a max-  
 133 imum value,  $\tau_{max}$ , at  $y/W = 0.375$  from the southern boundary ( $y = 0$ ). A hyper-  
 134 bolic tangent meridional temperature gradient is imposed on the top surface of the do-

main, with  $T_{min}$  at the southern boundary,  $T_{max}$  at the northern boundary and a change of temperature  $\Delta T = (T_{max} - T_{min})$  occurring at  $y = W/6$ .

No-slip and adiabatic boundary conditions are imposed at the base ( $z = 0$ ) and sides ( $y = 0, W$ ) of the model. The northern boundary in this model is closed, contrasting with past work that has used an open northern boundary (Abernathy et al., 2011; Munday et al., 2013). Adding an open northern boundary would increase the complexity of the current setup. The model is energetically closed without northward transport, providing valuable insight into the energy budget of the system, as discussed in Sohail et al. (2018). Hence, we focus on a simple channel model for this study. The zonal boundary conditions are periodic for the temperature and velocity. At the top surface, no stress and no flux conditions are imposed for the meridional and vertical velocities, respectively, and zonal wind stress is applied through the vertical shear of zonal velocity,  $\partial u / \partial z$ . The surface buoyancy gradient is imposed through a fixed temperature condition. Note that this boundary condition is similar to a relaxation temperature boundary condition with a zero relaxation time (i.e., a Dirichlet boundary condition). The grid resolution of  $[N_x, N_y, N_z] = 1024 \times 513 \times 257$  is clustered near the top, bottom and southern edge of the domain and is uniform in the  $x$ -direction. The grid resolves the local Kolmogorov and Batchelor scales and captures the top and bottom Ekman layer and Stewartson boundary layers (Kunnen et al., 2011). Three Gaussian ridges of height  $z/H = 0.2$  provide an idealised representation of basal topography.

The flow is characterised by a number of non-dimensional governing parameters: the Rayleigh number ( $Ra$ ), Ekman number ( $E$ ), Prandtl number ( $Pr$ ), wind-stress parameter ( $S$ ), non-dimensional beta-plane ( $\hat{\beta}$ ), and aspect ratios,  $B$  and  $D$ . These governing parameters are defined as:

$$Ra = \frac{g'W^3}{\nu\kappa}, E = \frac{\nu}{f_0W^2}, Pr = \frac{\nu}{\kappa}, S = \frac{\tau_{max}}{\rho_0g'H}, \hat{\beta} = \frac{\beta W}{f_0}, B = \frac{L}{W}, D = \frac{H}{W}, \quad (1)$$

where  $f_0$  is the Coriolis parameter at the southern boundary,  $\nu$  is the molecular viscosity,  $\kappa$  is the molecular diffusivity,  $\rho_0$  is the reference density, and  $\beta$  is the latitudinal variation of the Coriolis parameter,  $\beta = df/dy$ . We also define an external Rossby number,  $Ro = U/f_0W$  (where  $U$  is a characteristic velocity scale), to describe the relative strength of buoyancy and rotation. The dominant length-scale controlling convective instability in this system is the length along which the temperature gradient is imposed (Hughes & Griffiths, 2008). Therefore, in defining the Rossby number, and in all of the key non-dimensional parameters except  $S$ , the characteristic length scale used is  $W$ . There are several velocity scales available for use when defining the Rossby number. In order to express the Rossby number in terms of external parameters, we choose the convective velocity scale  $U \sim \sqrt{g'H}$  as the characteristic velocity. The response of the system is dominated by vertical advection due to convection, which can be represented by the velocity scale of a gravity current. Using the convective velocity scale, the Rossby number may be expressed as  $Ro = \sqrt{g'H}/f_0W = (RaE^2Pr^{-1}D)^{1/2}$ .

The DNS solves the incompressible, non-hydrostatic Navier-Stokes momentum equations with a Boussinesq approximation, linear equation of state, beta-plane assumption and heat and volume conservation in a rotating reference frame (see Sohail et al. (2018)). In this study, a hat denotes a non-dimensionalised quantity, such that  $\hat{t} = tU/W$ ,  $\hat{\mathbf{u}} = \mathbf{u}/U$ ,  $\hat{T} = T/\Delta T$ ,  $\hat{\rho} = \rho/\rho_0$  and  $[\hat{x}, \hat{y}, \hat{z}] = [x/L, y/W, z/H]$ .

Table 1 shows the relevant governing parameters for the suite of simulations conducted alongside a comparison with the Southern Ocean. We run four numerical simulations in which we vary wind stress,  $S$ , keeping all other non-dimensional parameters the same. In addition, we conduct one simulation with a reduced buoyancy forcing ( $Ra \sim 10^{10}$ ) and a dimensional surface wind stress  $\tau_{max}$  which is kept the same as Case B. In

Case	$Ra$	$S$	$E$	$Ro$
A	$1.125 \times 10^{12}$	0	$4 \times 10^{-7}$	0.12
B	$1.125 \times 10^{12}$	$4.44 \times 10^{-5}$	$4 \times 10^{-7}$	0.12
C	$1.125 \times 10^{12}$	$8.89 \times 10^{-5}$	$4 \times 10^{-7}$	0.12
D	$1.125 \times 10^{12}$	$1.77 \times 10^{-4}$	$4 \times 10^{-7}$	0.12
E	$3.75 \times 10^{10}$	$1.33 \times 10^{-3}$	$2 \times 10^{-6}$	0.11
SO	$1.2 \times 10^{25} - 1.9 \times 10^{26}$	$2.3 \times 10^{-6}$	$4.44 \times 10^{-14} - 1.78 \times 10^{-13}$	0.025

**Table 1.** The relevant dimensionless parameters for the suite of simulations conducted (A-E). Case SO represents the dimensionless parameters for the Southern Ocean, calculated in Sohail et al. (2018).

all cases,  $Pr = 5$ ,  $D = 0.4$  and  $B = 5$ . The maximum Rayleigh number in the model runs is about 10 orders of magnitude less than that expected for the Southern Ocean. That said, a Rayleigh number of  $Ra > 10^{11}$  is large enough to maintain turbulent convection over the portion of the top boundary where destabilizing buoyancy forcing is applied (Gayen et al., 2014). Therefore, Cases A-D lie in the turbulent convection regime, while Case E does not. In addition, the Rayleigh numbers achieved in these simulations are the maximum attainable given our computational resources. The depth-to-width aspect ratio,  $D$ , is still several orders of magnitude greater than the real ocean, as  $D$  must be chosen with the thermal boundary layer thickness (defined as the highly stratified region at the top of the water column,  $\delta_T$ ) in mind. Thermal boundary layer thickness increases with decreasing Rayleigh number, so the aspect ratio is selected such that  $\delta_T$  is much smaller than domain height (within the bounds of the grid resolution) for the range of  $Ra$  in this study.

All boundaries (save the top surface) are adiabatic, so at thermal equilibrium the net heat flux through the surface should be zero. Consequently, the system is considered to be in thermal equilibrium when the positive surface diffusive heat flux is within 5% of the negative surface diffusive heat flux, and the fluctuations in kinetic energy lie within 2% of the mean. All mean quantities, denoted by an overbar  $\overline{(-)}$ , are calculated by time-averaging over at least 45 buoyancy time-scales,  $\tau_b = \sqrt{W/g'}$ . Here,  $g'$  is the reduced gravity, defined as  $g' = g\alpha\Delta T$ , where  $\alpha$  is the coefficient of thermal expansion,  $g$  is the acceleration due to gravity and  $\Delta T$  is the maximum meridional temperature difference. Fluctuating terms, denoted by a prime  $(-)'$ , are the deviation from the time mean at any given time instant,  $(-)' = (-) - \overline{(-)}$ . Note that, in the DNS conducted here, turbulence, convection and baroclinic eddies have comparable length scales, so identifying the features individually is not possible. As a result, the term ‘fluctuating’ is used in this analysis as distinct from ‘eddy’, primarily due to the fact that all variability in the system, not just eddies, is captured by the fluctuating terms.

### 3 Results

The southern edge of the domain over which the unstable buoyancy forcing is imposed is characterised by vigorous turbulent convection (figure 1). The combined effect of the buoyancy forcing, in conjunction with the surface wind stress, steepens the isopycnals, increasing the available potential energy. In response to the enhancement of the density gradients in the system, the flow becomes baroclinically unstable, shedding coherent eddies. These baroclinic eddies migrate from the generation site, playing a major role in flattening the meridional density gradient over depth and impacting meridional and zonal transport (Karsten et al., 2002; Sohail et al., 2018). These processes are extremely important in driving Southern Ocean circulation, and are visible in the ide-

alised model studied here. The snapshot of vertical vorticity (top surface in figure 1) illustrates the presence of these multi-scale flow features. In the following sections we investigate the role of wind stress and buoyancy forcing on zonal and meridional transport in thermally equilibrated DNS solutions.

### 3.1 Zonal Transport

The zonal transport in the model is diagnosed by calculating the time-averaged area-integrated zonal velocity, given by:

$$\mathbf{T}_{zonal} = \frac{1}{L} \int_V \bar{u} dV. \quad (2)$$

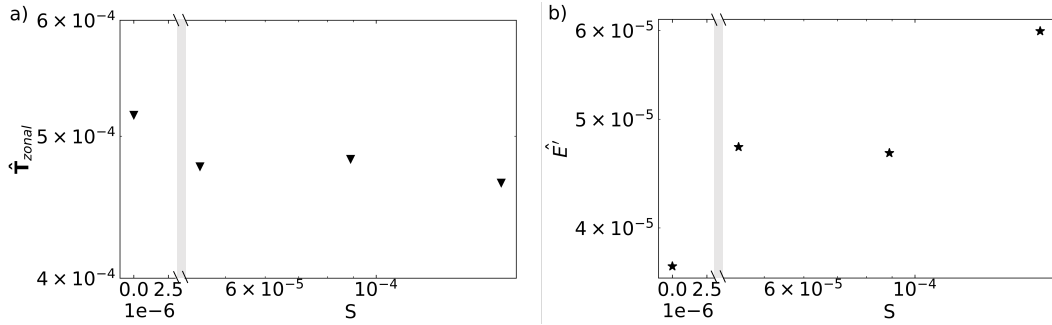


**Figure 2.** a) Zonal transport for Cases A - D for varying wind stress,  $S$ . Transport has been non-dimensionalised by  $\mathbf{T}_0 = W\sqrt{g'H^3}$ . b) Fluctuating kinetic energy for Cases A - D for varying wind stress,  $S$ . Kinetic energy has been non-dimensionalised by  $E_0 = g'H$ .

The zonal transport,  $\mathbf{T}_{zonal}$ , is compared across simulations to examine the sensitivity of  $\mathbf{T}_{zonal}$  to varying wind stress,  $S$ , as shown in figure 2a. Upon introducing a surface wind stress, the zonal transport decreases, becoming less sensitive with further increases in wind stress. This result is consistent with a large-scale ocean model study by Hogg and Munday (2014), who found that circumpolar transport decreases to an asymptotic limit at sufficiently high wind stress. The strength of zonal transport in the model is related to the meridional stratification by the thermal wind balance. The stratification is in turn affected by baroclinic instability, which works to remove thermal gradients (sources of available potential energy) in the flow. The indirect link between zonal transport and fluctuating flows may be further explored by analysing the fluctuating component of kinetic energy  $E' = 1/2(u'^2 + v'^2 + w'^2)$ . This definition of  $E'$  encompasses baroclinic eddies, convection and other variability, therefore providing *some* indication of eddy activity with the caveat that this may also include convection and turbulence. Figure 2b shows that  $\hat{E}'$  increases with higher wind stress, suggesting that fluctuating flows also increase with  $S$ . Wind stress enhances surface density gradients, which triggers baroclinic instability that flattens isopycnal slope in the stratified region. Therefore, there exists a competition between surface wind and baroclinic eddies in modifying the meridional stratification.

Figure 3 compares the change in isopycnal slope between case B (a ‘low’ wind stress case) and case D (a ‘high’ wind stress case). From figure 3a, the zonally-averaged isopycnal slope seems unchanged with increasing wind stress. Throughout the water column, and particularly near the strongly stratified surface, the buoyancy frequency is almost identical. Differences between the two cases do exist in the interior, but these are very small given the full range of buoyancy frequencies through depth (figure 3b). Therefore,

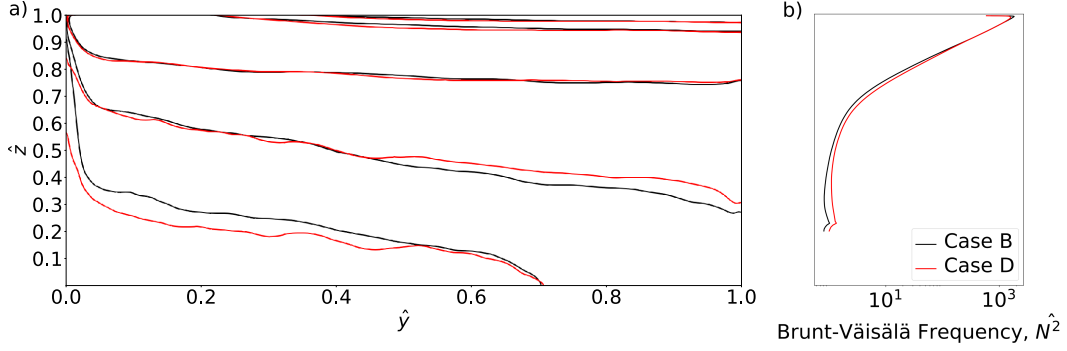


**Figure 3.** a) Time- and zonally-averaged isotherms for Cases B and D, where  $\hat{T} = [0.667, 0.432, 0.192, 0.187, 0.186]$  from top to bottom for Case B and  $\hat{T} = [0.667, 0.432, 0.199, 0.193, 0.192]$  from top to bottom for Case D. b) Zonally-, meridionally- and time-averaged non-dimensionalised buoyancy frequency,  $\hat{N}^2$ , for Cases B and D. Buoyancy frequency is non-dimensionalised by  $N_0^2 \approx 10^{-4}$ , the buoyancy frequency in the model interior. Values of  $\hat{N}^2$  are truncated below  $\hat{z} = 0.2$ , where topographic effects are present.

there is little net change in the meridional stratification, in part due to the increase in fluctuating flows (figure 2b). In the limit where all scales of motion are fully characterised, fluctuating flows (including convection and eddies) play a role in regulating ACC transport within the range of wind stress studied here. This trend is consistent with previous studies using larger scale ocean models (Morrison & Hogg, 2013; Hogg et al., 2015; Bishop et al., 2016).

### 3.2 Overturning Circulation

We diagnose the impact of buoyancy and small-scale flows on overturning circulation in the model using a depth-density streamfunction. The depth-density streamfunction represents the total vertical transport of fluid with higher density than a given value,  $\rho^*$ , at a constant depth (see Nurser and Lee (2004); Nycander et al. (2007)). The depth-density streamfunction at  $\rho = \rho^*$  is defined as:

$$\Psi(\rho^*, z) = -\frac{1}{\Delta t} \int \int \int_{\rho^* \geq \rho} w(x, y, z, t) dx dy dt \quad (3)$$

where  $w$  is the vertical velocity,  $\Delta t$  is the time range over which the streamfunction is averaged,  $\rho$  is the density at each location and  $\rho^*$  is the ‘binned’ density classes. By construction, the depth-density streamfunction is a volume flux. Here, all streamfunctions are non-dimensionalised by  $\Psi_0 = WL\sqrt{g'H}$ .

The depth-density streamfunction is a useful tool to distinguish between thermally direct and thermally indirect overturning (Nycander et al., 2007). The thermally direct overturning, which is driven by buoyancy forcing, is characterised by sinking negatively buoyant fluid at the southern edge of the domain and rising positively buoyant fluid throughout the interior, resulting in a negative cell. On the other hand, thermally indirect overturning, which is driven by mechanical forcing, is characterised by sinking positively buoyant fluid and rising negatively buoyant fluid, resulting in a positive cell. The thermally indirect overturning is primarily driven by Ekman transport induced by surface wind stress. Using a depth-density streamfunction yields a number of benefits over other diagnostic measures, including the ‘traditional’ depth-latitude streamfunction and the density-latitude streamfunction. In a re-entrant channel system, a depth-latitude streamfunction would show full-depth cells corresponding to Ekman transport and transient barotropic eddies. Therefore, this streamfunction would not yield any meaningful information about the

280 buoyancy- and wind-driven overturning circulation. The density-latitude streamfunction  
 281 also does not yield physically meaningful transport, potentially due to the presence of  
 282 statically unstable flows with strong vertical velocities and a large volume of dense fluid  
 283 at the surface. The depth-density streamfunction accurately represents overturning in  
 284 statically unstable flows, and may be used to analyse meridional and zonal flow in a basin  
 285 with no eastern and western boundaries (such as the Southern Ocean), making it an ideal  
 286 choice for this analysis (Zika, Sommer, et al., 2013; Zika, Sijp, & England, 2013).

287 The depth-density streamfunction can be further mapped onto pseudo-latitude space  
 288 to produce a meridional section of the overturning circulation, where, in a Cartesian grid,  
 289 the pseudo-latitude,  $\mathbf{Y}(\rho^*, z)$ , is given (following Zika, Sommer, et al. (2013)) by:

$$\mathbf{Y}(\rho^*, z) = \frac{1}{\Delta t \Delta x} \int \int \int_{\rho^* \geq \rho} dx dy dt \quad (4)$$

290 The pseudo-latitude,  $\mathbf{Y}$  is then mapped onto the entire latitudinal extent of the domain  
 291 through normalisation:  $(\mathbf{Y}/(y_{max}-y_{min}))-1$ . When mapped onto depth-latitude space,  
 292 the streamfunction enables a simple visualisation of the spatial extent of the two over-  
 293 turning cells.

294 Prior work has highlighted the importance of models which resolve fine-scale flows  
 295 in clarifying the impact of surface wind stress and buoyancy on Southern Ocean trans-  
 296 port. A major motivation for the present study is to identify the influence of the pres-  
 297 ence of turbulence and convection on volume transport. To that end, we compare the  
 298 depth-density streamfunction for two cases with differing buoyancy forcing but the same  
 299 surface wind stress, Cases B and E. Gayen et al. (2014) showed that turbulent convec-  
 300 tion is triggered when the Rayleigh number is above a critical threshold,  $Ra \sim 10^{11}$ .  
 301 Case B has a Rayleigh number above this critical threshold, and so is characterised by  
 302 turbulent convection, whilst case E has a Rayleigh number below the critical threshold.  
 303 Therefore, a comparison between these two cases elucidates the impact of turbulence on  
 304 modifying the overturning circulation.

305 The onset of turbulent convection in Case B (hereafter the ‘turbulent’ case) results  
 306 in significant changes to the overturning circulation (figure 4). The abyssal overturning  
 307 (in blue) is larger in strength and extent in the turbulent case as compared with the weaker  
 308 and less well-defined cell in case E (hereafter the ‘non-turbulent’ case). Furthermore, the  
 309 northward extension of the abyssal cell in the turbulent case is not as evident in the non-  
 310 turbulent case. “Northward” in the context of the overturning circulation refers to the  
 311 region north of the southern boundary, and does not imply a specific latitude in the South-  
 312 ern Ocean. The northwards extension of the abyssal cell in the presence of turbulent con-  
 313 vection suggests that turbulence may play a leading role in connecting the overturning  
 314 circulation with the northern hemisphere in the real ocean. The abyssal overturning also  
 315 strengthens with the presence of turbulence - the maximum abyssal overturning in the  
 316 turbulent case (measured at  $\hat{\mathbf{Y}} = 0.5$ ) is 13 times greater than that in the non-turbulent  
 317 case. On the other hand, the upper overturning cell (in red) is weaker and isolated to  
 318 within the surface boundary layer in the turbulent case. In the presence of turbulence,  
 319 the maximum upper overturning (measured at  $\hat{\mathbf{Y}} = 0.5$ ) drops by 80%. This result sug-  
 320 gests that turbulence may play a role in modifying the strength and extent of the over-  
 321 turning, enhancing the abyssal cell while weakening the upper cell.

322 The difference in magnitude and spatial extent of the overturning circulation may  
 323 also be due to the difference in buoyancy forcing between the turbulent and non-turbulent  
 324 case. In order to parse between the effects of turbulence and the different buoyancy forc-  
 325 ing, it is necessary to run an additional simulation with a buoyancy forcing greater than  
 326 the turbulent case (Case B). However, this is not computationally feasible, limiting our  
 327 ability to decisively conclude how much of a role turbulence is playing in the change in  
 328 overturning in figure 4. Regardless, it is clear that increasing the buoyancy forcing re-

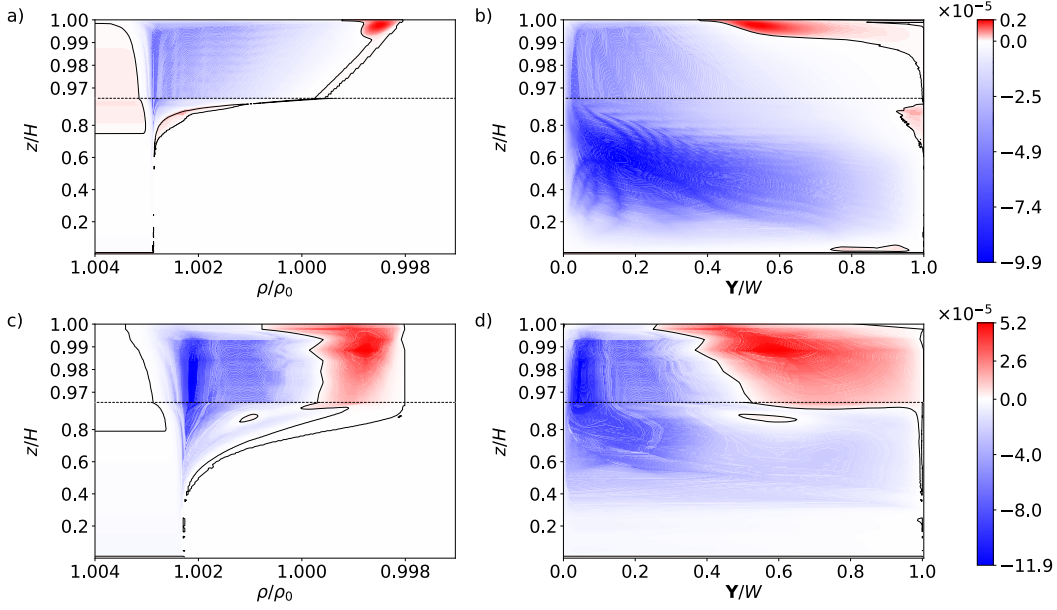


**Figure 4.** Non-dimensionalised depth-density streamfunctions for a) Case B, a ‘turbulent’ simulation, and b) Case E, a ‘non-turbulent’ simulation; c) and d) Same as a) and b) but remapped onto depth-latitude space. The thermal boundary layer region (in the top  $\hat{z} \approx 0.03$  of the domain) has been expanded in these plots. The streamfunctions have been non-dimensionalised by  $\Psi_0 = WL\sqrt{g'H}$ .

sults in significant modifications to the flow, and some part of that is due to turbulence in the system. Hence, it remains an imperative to run a turbulence-resolving simulation in analysing the sensitivity of the meridional overturning to surface forcing.

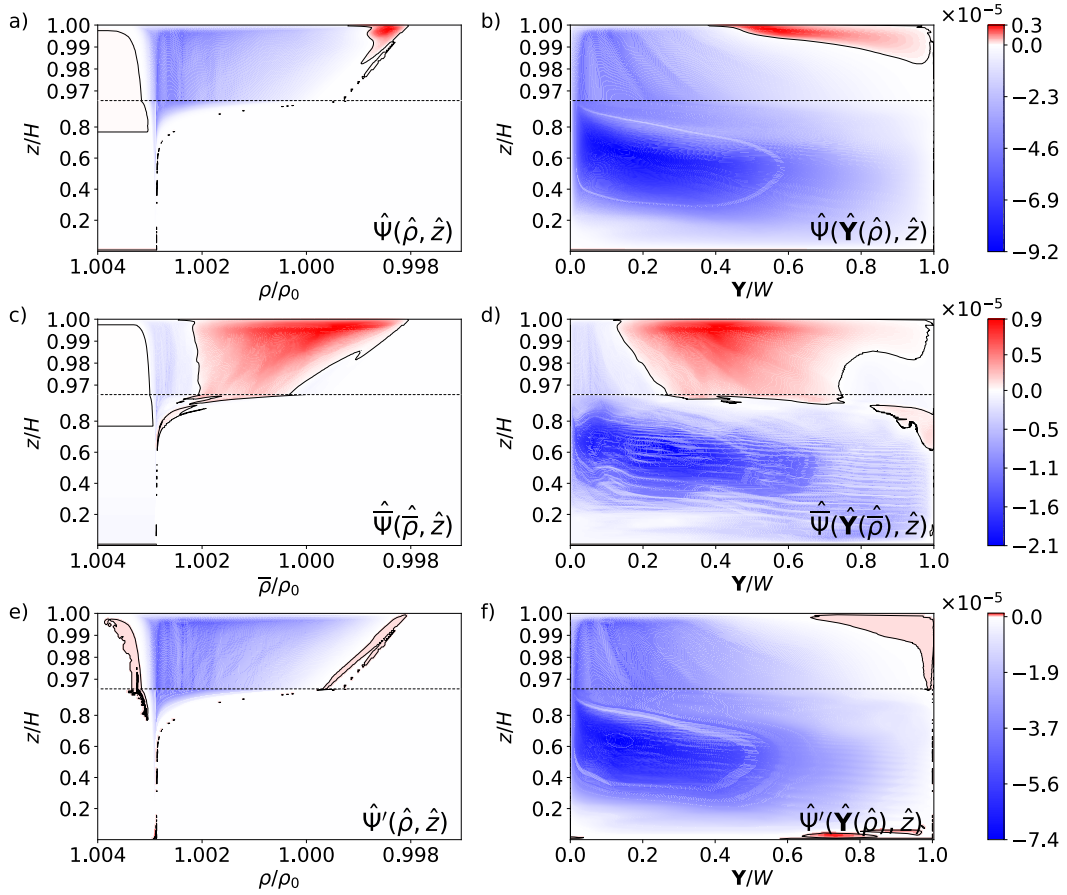
In order to gauge the sensitivity of mean and fluctuating flow features to wind stress, we further decompose the depth-density streamfunction based on the mean and fluctuating components of the velocity. The mean streamfunction is defined, following Zika, Sommer, et al. (2013), as:

$$\bar{\Psi}(\bar{\rho}, z) = - \int \int \int_{\rho_{bin} \geq \bar{\rho}} \bar{w}(x, y, z) dx dy, \quad (5)$$

where  $\bar{w}$  is the time-averaged vertical velocity and  $\bar{\rho}$  is the time-averaged density field. The mean streamfunction as defined here is distinct from the mean Eulerian streamfunction diagnostic used by J. Marshall and Radko (2003) and Abernathy et al. (2011). We instead employ the mean framework used by Zika, Sommer, et al. (2013). The fluctuating depth-density streamfunction is calculated from the residual overturning streamfunction (as defined by (3)) and the mean overturning streamfunction (as defined by (5)) using:

$$\Psi'(\rho, z) = \Psi(\rho, z) - \bar{\Psi}(\bar{\rho}, z). \quad (6)$$

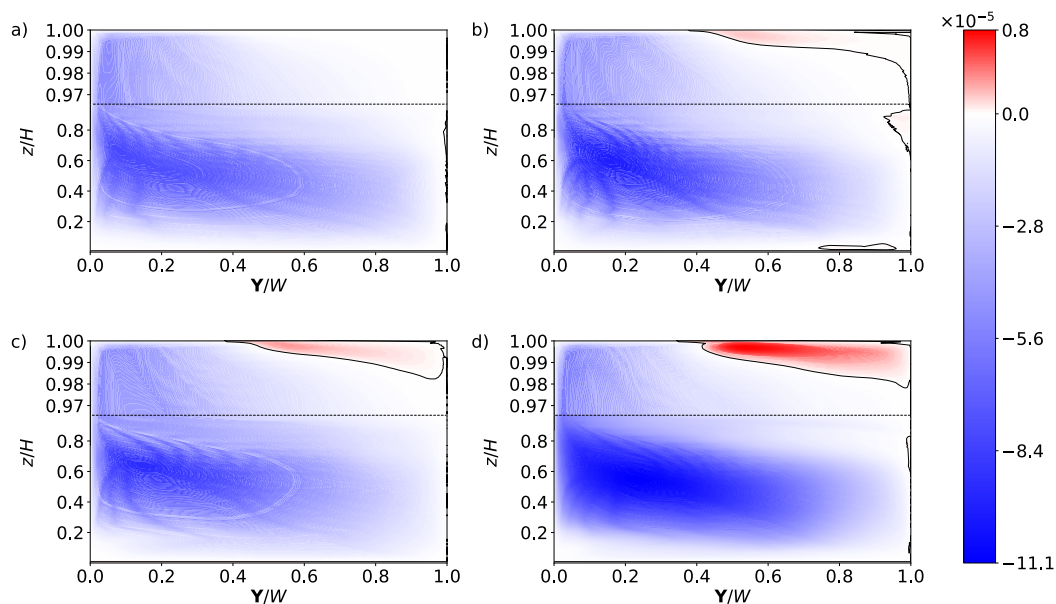
The mean and fluctuating streamfunctions are remapped onto depth-latitude space to show the spatial extent of these components. Figure 5 shows the residual, mean and fluctuating overturning streamfunctions for a moderate wind stress case (Case C). The residual depth-density streamfunction (figure 5a, b) reveals a lower overturning cell which is relatively strong and occupies a significant meridional section of the domain. The upper cell is weak and inside the thermal boundary layer.



**Figure 5.** Depth-density streamfunctions for Case C. a) Residual depth-density streamfunction,  $\hat{\Psi}(\hat{\rho}, \hat{z})$ ; c) Mean depth-density streamfunction,  $\hat{\Psi}(\bar{\rho}, \hat{z})$ ; e) Fluctuating depth-density streamfunction,  $\hat{\Psi}'(\hat{\rho}, \hat{z})$ ; b), d) and f) Same as a), c) and e) above but remapped onto depth-latitude space. The thermal boundary layer region (in the top  $\hat{z} \approx 0.03$  of the domain) has been expanded in these plots.

Upon decomposition into the constituent mean and fluctuating parts, the relative contribution of different scales of flow to the overturning becomes more apparent. As shown in figure 5(c, d), the upper cell is dominated by the mean flow features, namely, by time-invariant Ekman transport. The lower cell in the mean overturning is dominated by the direct, buoyancy driven flow, which is associated with the presence of a persistent plume at the southern boundary (Sohail et al., 2018). The mean upper cell extends through the surface boundary layer, penetrating up to  $\hat{z} \approx 0.9$ . The majority of volume flux in the lower cell is due to fluctuating flow processes, as shown in figure 5(e, f), where the abyssal cell dominates the fluctuating flow field. Therefore, the upper overturning cell exists primarily due to mean flow (from imposed wind stress), while the lower overturning cell is a consequence of small scale time variant features (such as convection and eddies). The mean upper overturning fills the depth of the surface boundary layer, but is largely cancelled out by the fluctuating lower overturning cell when visualising the residual overturning. The resulting upper overturning cell (in figure 5b) is weak and surface-isolated.

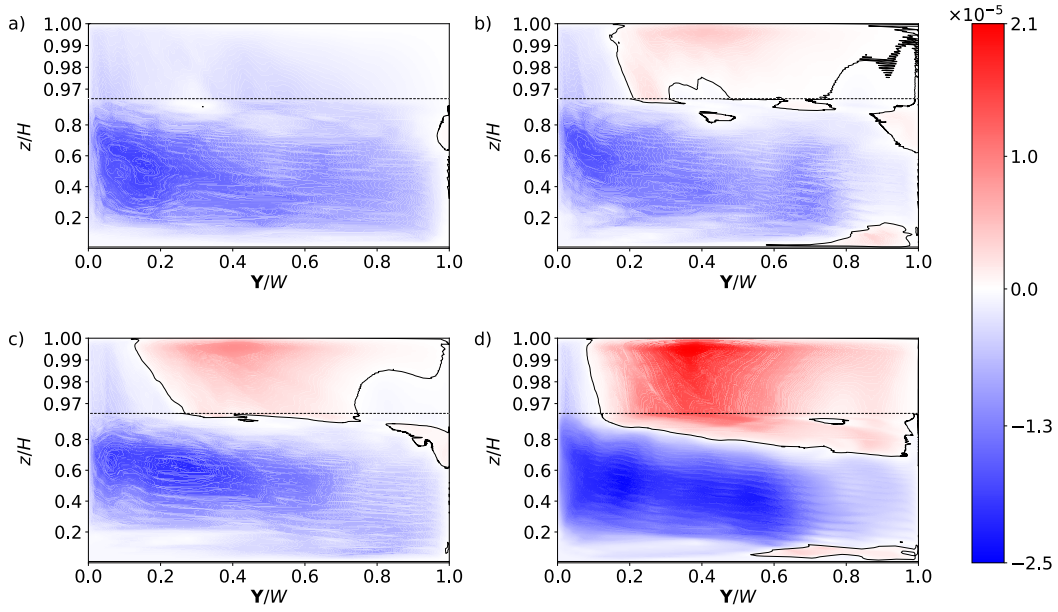
We now compare across the suite of simulations A - D to analyse the spatial sensitivity of the residual, mean and fluctuating overturning cells to increasing wind stress.



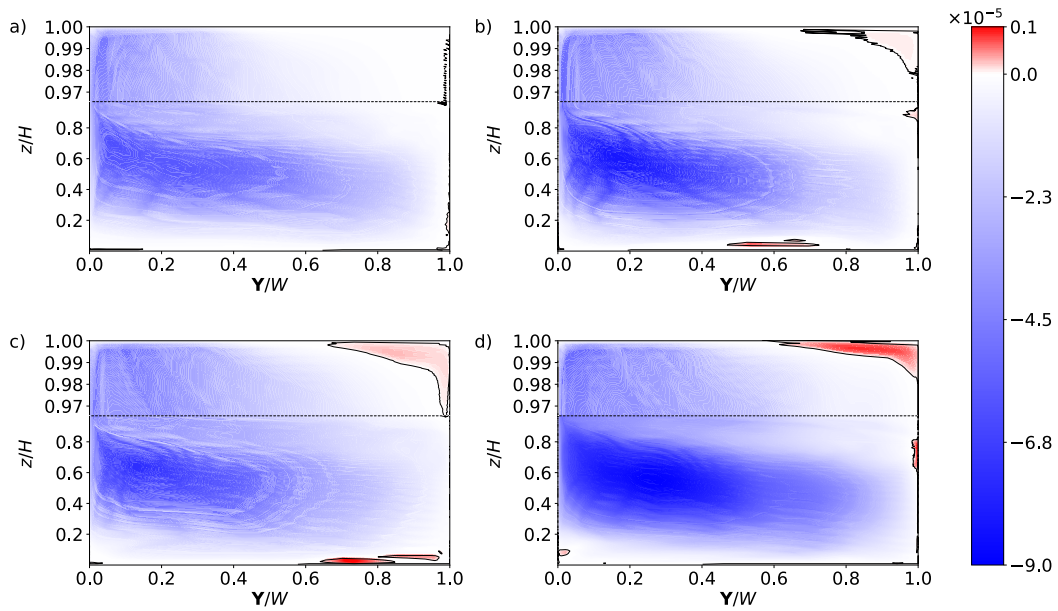
**Figure 6.** a) - d) Residual overturning streamfunctions  $\hat{\Psi}(\hat{\mathbf{Y}}(\hat{\rho}), \hat{z})$ , for Cases A to D respectively. The thermal boundary layer region (in the top  $\hat{z} \approx 0.03$  of the domain) has been expanded in these plots.

Figure 6 (calculated from equation (3) and mapped onto depth-latitude co-ordinates) shows the sensitivity of the upper and lower residual overturning to increasing wind stress. Case A (figure 6a) has no wind forcing, and has no significant thermally indirect (wind-driven) overturning. As wind stress increases from cases B to D, the thermally indirect upper cell increases in strength and spatial extent. However, the cell remains in the surface boundary layer, and is weaker than the abyssal cell. A possible cause of the shallow upper cell in this model may be the closed northern boundary in our model, which inhibits any heat or volume exchange through the northern boundary. The northern boundary consequently may limit the size of the upper overturning cell as it deepens northwards. The lower cell, on the other hand, extends throughout the depth and meridional extent of the model for all cases. Strengthening winds result in the strengthening of the abyssal cell further northwards. This northward strengthening (particularly evident in case D, figure 6d) would modify the overturning in the northern hemisphere in a global model. The relative contribution of the mean and fluctuating circulation in the residual overturning can also be analysed.

The mean overturning streamfunction (figure 7), on the one hand, is highly sensitive to changing winds. Case A (figure 7a) has a mean overturning which is solely thermally-direct, again due to the absence of a surface wind stress. Any thermally-indirect transport may be due to time-averaging or truncation errors in the streamfunction calculation. Cases B - D, however, have a mean upper cell that increases in depth and strength over the range of  $S$  studied, as shown in figure 7(b-d). As  $S$  increases, the mean upper cell intensifies and deepens, until it occupies about 10% of the domain in Case D (figure 7d). Whilst the upper cell extends across the width of the domain at the most extreme values of  $S$ , the strongest upper overturning is seen in the southern 3/4 of the domain, where the zonal wind stress is imposed. The shape of the mean abyssal overturning does not appear to change significantly with increasing wind stress. However, the region of high overturning in the lower cell does stretch northward, as observed in the residual plots. Hence, mean flows expand the upper overturning cell and extend the mean abyssal overturning northwards.



**Figure 7.** a) - d) Mean overturning streamfunctions  $\widehat{\Psi}(\widehat{\mathbf{Y}}(\widehat{\rho}), \widehat{z})$ , for Cases A to D respectively. The thermal boundary layer region (in the top  $\widehat{z} \approx 0.03$  of the domain) has been expanded in these plots.



**Figure 8.** a) - d) Fluctuating overturning streamfunctions  $\widehat{\Psi}'(\widehat{\mathbf{Y}}(\widehat{\rho}), \widehat{z})$ , for Cases A to D respectively. The thermal boundary layer region (in the top  $\widehat{z} \approx 0.03$  of the domain) has been expanded in these plots.

95 The spatial extent of the fluctuating streamfunction (figure 8), on the other hand,  
 96 appears to be less sensitive to wind stress. Fluctuating terms primarily contribute to the  
 397 abyssal overturning. The abyssal cell extends through the full depth for all cases, and  
 398 the shape of the cell does not vary significantly. Similar to the mean overturning, the  
 99 abyssal cell stretches northwards as wind stress increases. Fluctuating flows therefore

400 maintain the same general shape of the abyssal cell regardless of wind stress, while strength-  
 401 ening further northwards with increased winds.

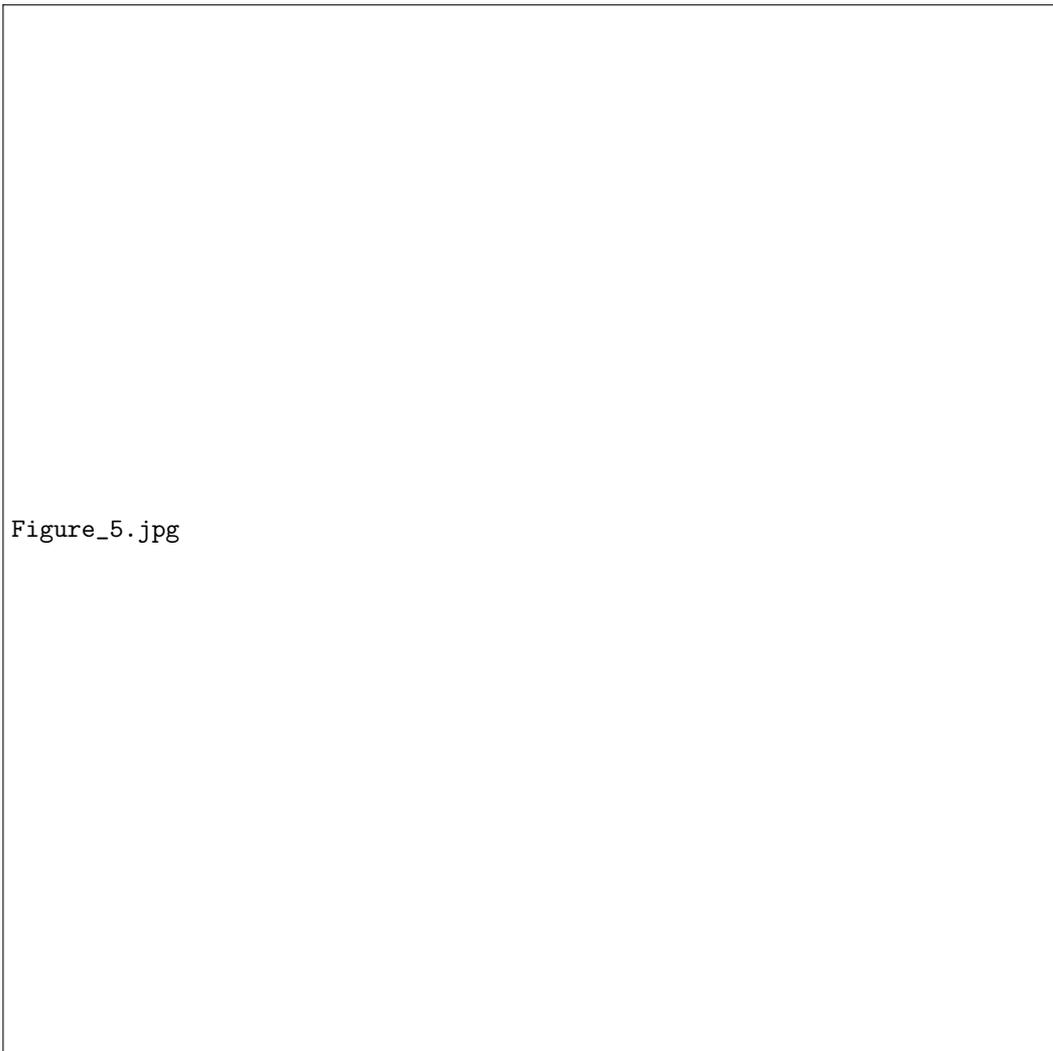


**Figure 9.** Maximum upper and lower overturning depth-density streamfunctions as a function of wind stress parameter,  $S$ , measured at  $\hat{Y} = 0.5$ . a) Upper overturning depth-density streamfunction maxima,  $\hat{\Psi}_{upper}$  split into residual, fluctuating and mean components, and b) Lower overturning depth-density streamfunction maxima,  $\hat{\Psi}_{lower}$  split into residual, fluctuating and mean components, with increasing  $S$ . The fluctuating upper overturning maximum is measured as the fluctuating overturning at the location of the maximum residual upper overturning. The absolute value of the fluctuating upper overturning is plotted here.

02 The spatial plots in figures 6, 7 and 8 show the sensitivity of the *extent* of the over-  
 03 turning cell to increasing wind. To quantify the sensitivity of the *strength* of the over-  
 404 turning cell to wind stress, we plot the maximum lower and upper residual, mean and  
 05 fluctuating streamfunctions as a function of wind stress,  $S$ , in figure 9. The residual, mean  
 06 and fluctuating upper overturning cells increase in strength with increasing  $S$  (figure 9a).  
 407 As wind stress strengthens, the Ekman transport in the surface boundary layer increases,  
 408 in turn enhancing the upper overturning. When decomposed into mean,  $\bar{\Psi}(\mathbf{Y}(\rho), z)$ , and  
 09 fluctuating,  $\Psi'(\mathbf{Y}(\rho), z)$ , components, the flow features that control the rate of upper over-

410 turning become apparent. The mean upper overturning quickly strengthens with increas-  
 411 ing  $S$ . The fluctuating component of the upper overturning is calculated as the fluctu-  
 412 ating overturning at the location of the maximum residual upper overturning. The fluctu-  
 413 ating upper overturning is negative (its absolute value is plotted in figure 9a), and increas-  
 414 es with  $S$ , but is much smaller than the mean component. This is because the fluctu-  
 415 ating overturning is relatively weak in the region where the mean upper overturning  
 416 exists, so the counter-rotating fluctuating flows do not cancel out the relatively strong  
 417 mean overturning. So, the overturning circulation in the upper cell is minimally eddy  
 418 compensated, and is dominated by mean flow.

419 The residual and fluctuating lower overturning streamfunctions increase with increas-  
 420 ing  $S$ , as shown in figure 9b. We have established that fluctuating flows increase  
 421 with increasing  $S$  (see figure 2b), as a consequence of the enhancement of available po-  
 422 tential energy due to increasing surface winds (Karsten et al., 2002; Sohail et al., 2018).  
 423 These fluctuations reduce the mean available potential energy in the system, fluxing heat  
 424 across and along mean isopycnals and also fluxing volume from warm to cold regions.  
 425 Therefore, the thermally direct fluctuating abyssal overturning increases, reflecting the  
 426 higher turbulent activity. The increase in fluctuations also has an impact on the mean  
 427 abyssal overturning, which also shows a positive correlation with  $S$ . The enhanced vol-  
 428 ume flux from north to south is arrested by the presence of a wall at the southern bound-  
 429 ary. The fluid then moves downwards in the form of a plume. This boundary plume is  
 430 spatially-invariant, so increased volume flux due to the plume will be captured by the  
 431 mean streamfunction.

432 Overall, the residual upper overturning cell in this model is at least one order of  
 433 magnitude smaller than the residual lower overturning. The mean lower overturning is  
 434 of a similar order of magnitude as the mean upper overturning, so the difference between  
 435 the transport arises from the fluctuating component of the lower and upper cells, which  
 436 is vastly different. Whilst the residual upper overturning increases with  $S$ , it remains weaker  
 437 than the abyssal overturning, even in the most extreme wind stress case (Case D).

### 438 3.3 Scaling

439 We develop a scaling theory to predict the trends in overturning sensitivity in a  
 440 variety of forcing conditions. This scaling theory is developed in terms of the governing  
 441 parameters in (1), and validated with the model output in figure 9. The upper compo-  
 442 nent ( $\Psi_{upper}$ ), is difficult to validate with a theoretical scaling. From figure 5, the mean  
 443 upper overturning cell occupies the same space as the fluctuating lower cell, leading to  
 444 a shallow residual upper overturning cell. Hence, the residual and fluctuating upper over-  
 445 turning streamfunctions cannot be accurately predicted using a theoretical scaling. In  
 446 contrast, the mean upper overturning, shown in figure 7, is a direct consequence of Ek-  
 447 man transport, and can be described in terms of a theoretical scaling.

448 The depth-density streamfunction represents the volume flux in the system due to  
 449 the buoyancy- and wind-forcing. The scaling for the streamfunction  $\Psi$  is  $\Psi \sim ULW$ ,  
 450 where  $U$  is the characteristic vertical velocity. In the case of the upper cell, the charac-  
 451 teristic velocity,  $U$ , is a direct consequence of the wind action, and can be approximated  
 452 by the Ekman pumping in the system,  $w_E$ . The Ekman pumping scales as  $w_E \sim \tau_{max}/\rho_0 f_0 W$ ,  
 453 resulting in a scaling of  $\hat{\Psi}_{upper}$ :

$$454 \hat{\Psi}_{upper} = \frac{\bar{\Psi}_{upper}}{\Psi_0} \sim \frac{\tau_{max}}{\rho_0 f_0 W \sqrt{g'H}} = c_{\bar{\Psi}_{wind}} S Ro \quad (7)$$

455 where  $c_{\bar{\Psi}_{upper}} = 0.74$  from the model results. This scaling is plotted against the model  
 output in figure 9, and shows a good correlation with the model. The linear scaling iden-

456 tified here aligns with scaling analyses presented in previous eddy-resolving ocean mod-  
457 els (e.g., Karsten et al. (2002); Viebahn and Eden (2010); Abernathy et al. (2011)).

## 58 4 Discussion and Conclusions

59 We use a turbulence-resolving idealised model with surface wind and buoyancy forc-  
460 ing (reminiscent of the Southern Ocean), to identify the impact of fine-scale turbulence,  
461 convection and eddy activity on volume transport. We also investigate the sensitivity  
462 of the meridional overturning and zonal transport to increasing surface wind stress across  
463 a suite of simulations.

64 The zonal transport in the model, analogous to ACC transport, is largely insen-  
465 sitive to increasing wind stress, aligning with findings from high-resolution idealised stud-  
66 ies (Munday et al., 2013; Morrison & Hogg, 2013). This insensitivity can be attributed  
467 to the enhancement of baroclinic eddies and convection in the system, which work to flat-  
468 ten isopycnal surfaces. As a consequence, mean density structures (with gradients in both  
469 the horizontal and vertical direction) are similar for all wind stress cases, and impose the  
70 same thermal wind balance (Hogg, 2010). As a result of the insensitivity of mean den-  
471 sity structures to wind, the zonal transport also remains insensitive to wind. The fact  
72 that the sensitivity of the zonal transport matches modelling and observational estimates  
473 provides confidence that the idealised model lies in the correct regime.

474 We find that the presence of turbulence enhances abyssal overturning, while sup-  
75 pressing the upper overturning cell in the model. The enhancement of convectively-driven  
476 diapycnal mixing (Sohail et al., 2018) in the abyssal cell may trigger increased transport,  
477 pushing the upper cell towards the surface and further north. We decompose the over-  
78 turning circulation into mean and fluctuating components using a residual streamfunc-  
479 tion formulation. The present study finds that the upper cell in the model is minimally  
30 eddy compensated when convection and turbulence are fully resolved. Therefore, the mean  
481 upper overturning streamfunction is much larger than the fluctuating upper streamfunc-  
482 tion. Therefore, the residual upper streamfunction is set primarily by the mean wind forc-  
33 ing and so is highly sensitive to wind stress. These results are consistent with the hypoth-  
484 esis that the strength and spatial extent of the upper overturning in the Southern Ocean  
485 may be set primarily by the mean flow triggered by surface winds.

486 In this model, the lower cell is much stronger, both in magnitude and in spatial ex-  
487 tent, than the upper cell. The abyssal transport appears to be dominated by fluctuat-  
88 ing flow features (i.e. convection, turbulence and eddies). These fluctuating features in-  
489 crease in response to increasing wind stress, effectively fluxing volume from north to south,  
as well as downwards. These fluctuating lateral and vertical volume fluxes lead to a strength-  
491 ening of the fluctuating abyssal overturning, and consequently the residual abyssal over-  
92 turning cell, with intensifying wind stress,  $S$ . Driven by the mean plume in the convective  
93 region along the southern boundary, the mean abyssal transport also shows a posi-  
494 tive correlation with increasing wind stress. However, the mean abyssal overturning re-  
195 mains much weaker than the fluctuating overturning. We conclude that fluctuating fea-  
36 tures play a major role in controlling the lower overturning circulation. These results fur-  
497 ther emphasize the importance of accurately characterising small-scale flow features in  
498 studies of Southern Ocean transport. By providing an indication of volume transport  
39 in the limit where all scales of motion are resolved, the model results help to guide fu-  
500 ture high-resolution modelling studies. We develop a scaling theory to predict the strength  
501 of the mean upper overturning in a number of flow regimes. This scaling theory predicts  
02 a linear sensitivity of the mean component of the upper cell to surface wind stress, match-  
503 ing previous studies (Karsten et al., 2002; Viebahn & Eden, 2010; Abernathy et al., 2011).

504 There are a number of assumptions and limitations to the present study which may  
05 be improved upon in the future. Whilst the DNS fully resolves all of the ocean dynam-

506 ics, from the planetary scale to turbulent dissipation scales, it does so within a much re-  
 507 duced range of length scales. We therefore keep in mind the possibility that the reduced  
 508 separation of length scales may lead to different interactions in the model output. In ad-  
 509 dition, future modelling studies may include an open northern boundary, either by in-  
 510 clusion of interhemispheric circulation, following Munday et al. (2013) and Wolfe and  
 511 Cessi (2011) or by imposing a realistic stratification, following Abernathy et al. (2011).  
 512 Increasing model complexity beyond this, such as the addition of a continental slope (as  
 513 studied by Stewart and Thompson (2013)) or Antarctic Peninsula (see Hogg and Mun-  
 514 day (2014)) can also be considered to more accurately represent meridional overturning.  
 515 The results hint at the need to better represent convection and turbulence in large-scale  
 516 models to accurately capture the (relatively large) AABW formation and abyssal cell.  
 517 Interhemispheric influences and other additional complexities are therefore reserved for  
 518 future modelling studies.

### 519 Acknowledgments

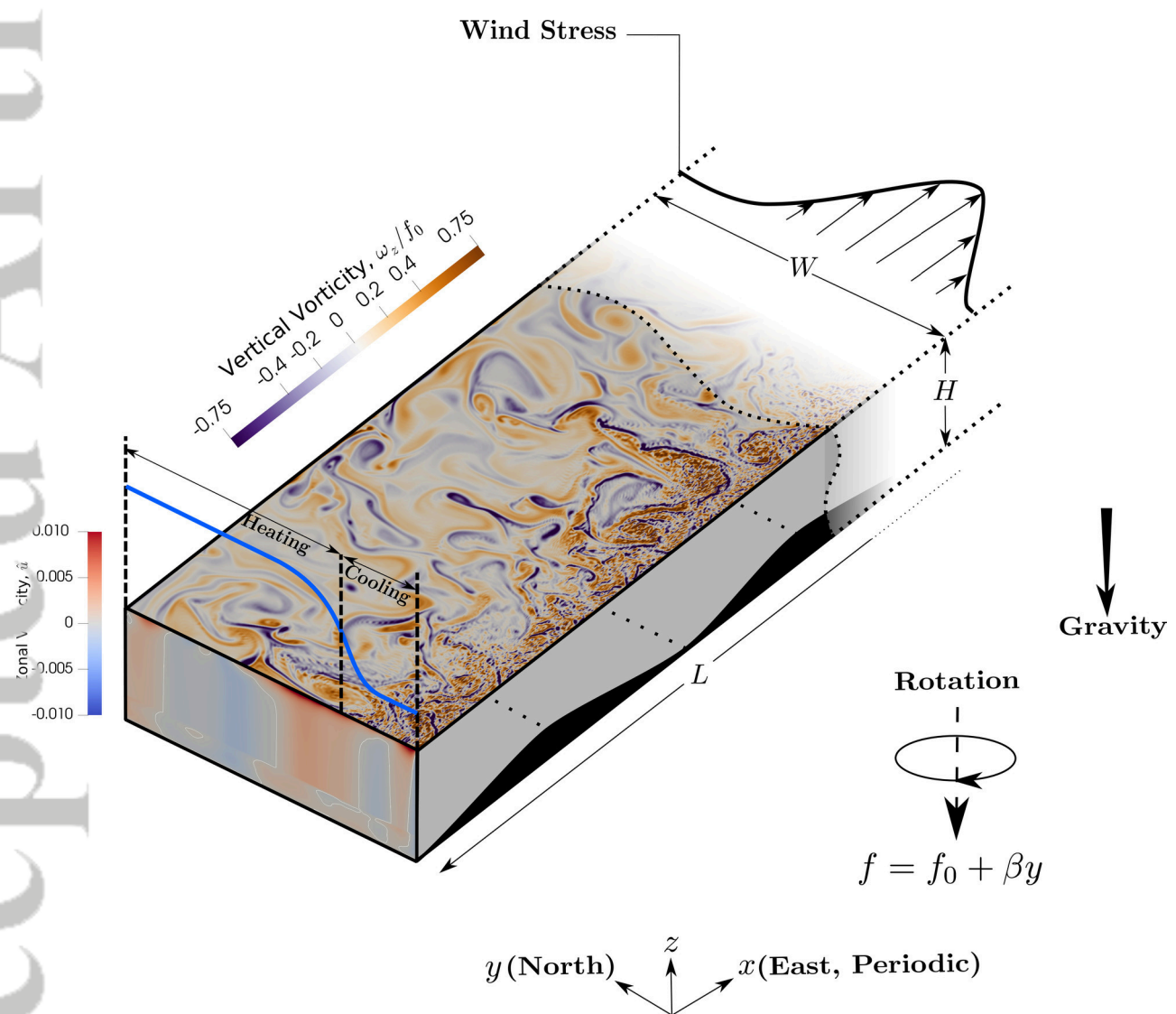
520 Numerical simulations were conducted on the Australian National Computational In-  
 521 frastructure (NCI), ANU, which is supported by the Commonwealth of Australia. This  
 522 research was supported by the Australian Research Council (ARC) grant DP140103706.  
 523 B.G. was supported by the R. J. L. Hawke Fellowship. We are grateful for the advice  
 524 and direction provided by R. W. Griffiths in earlier versions of this paper. We also thank  
 525 two anonymous reviewers for their constructive feedback and advice. Data supporting  
 526 the results may be found in Sohail et al. (2018) and in the supporting information.

### 527 References

- 528 Abernathy, R., Marshall, J., & Ferreira, D. (2011). The dependence of Southern  
 529 Ocean meridional overturning on wind stress. *Journal of Physical Oceanogra-*  
 530 *phy*, *41*, 2261-2278.
- 531 Barkan, R., Winters, K. B., & Smith, S. G. L. (2015, January). Energy cascades  
 532 and loss of balance in a reentrant channel forced by wind stress and buoyancy  
 533 fluxes. *Journal of Physical Oceanography*, *45*, 272-293.
- 534 Bishop, S. P., Gent, P. R., Bryan, F. O., Thompson, A. F., Long, M. C., & Aber-  
 535 nathy, R. (2016, May). Southern Ocean overturning compensation in an  
 536 eddy-resolving climate simulation. *Journal of Physical Oceanography*, *46*,  
 537 1575-1592.
- 538 Cai, W., & Baines, P. G. (1996, June). Interactions between thermohaline- and  
 539 wind-driven circulations and their relevance to the dynamics of the Antarctic  
 540 Circumpolar Current, in a coarse-resolution global ocean general circulation  
 541 model. *Journal of Geophysical Research*, *101*(C6), 14073 - 14093.
- 542 Farneti, R., Delworth, T. L., Rosati, A. J., Griffies, S. M., & Zeng, F. (2010). The  
 543 role of mesoscale eddies in the rectification of the Southern Ocean response to  
 544 climate change. *Journal of Physical Oceanography*, *40*, 1539 - 1557.
- 545 Gayen, B., Griffiths, R. W., & Hughes, G. O. (2014). Stability transitions and tur-  
 546 bulence in horizontal convection. *Journal of Fluid Mechanics*, *751*, 698-724.
- 547 Hande, L. B., Siems, S. T., & Manton, M. J. (2012, June). Observed trends in wind  
 548 speed over the Southern Ocean. *Geophysical Research Letters*, *39*(L11802), 1 -  
 549 5.
- 550 Henning, C. C., & Vallis, G. K. (2005). The effects of mesoscale eddies on the strat-  
 551 ification and transport of an ocean with a circumpolar channel. *Journal of*  
 552 *Physical Oceanography*, *35*, 880-896.
- 553 Hieronymus, M., Nycander, J., Nilsson, J., Döös, K., & Hallberg, R. W. (2019,  
 554 February). Oceanic overturning and heat transport: The role of background  
 555 diffusivity. *Journal of Physical Oceanography*, *32*, 701 - 716.
- 556 Hogg, A. M. (2010). An Antarctic Circumpolar Current driven by surface buoyancy

- 557 forcing. *Geophysical Research Letters*, *37*.
- 558 Hogg, A. M., Meredith, M. P., Chambers, D. P., Abrahamson, E. P., Hughes, C. W.,  
559 & Morrison, A. K. (2015). Recent trends in the Southern Ocean eddy field.  
560 *Journal of Geophysical Research: Oceans*, 257-267.
- 561 Hogg, A. M., & Munday, D. R. (2014). Does the sensitivity of Southern Ocean  
562 circulation depend upon bathymetric details? *Phil. Trans. R. Soc. A*,  
563 *372*(20130050).
- 564 Hogg, A. M., Spence, P., Saenko, O., & Downes, S. M. (2017). The energetics of  
565 Southern Ocean upwelling. *Journal of Physical Oceanography*, *47*, 135-153.
- 566 Howard, E., Hogg, A. M., Waterman, S., & Marshall, D. P. (2015). The injection of  
567 zonal momentum by buoyancy forcing in a Southern Ocean model. *Journal of*  
568 *Physical Oceanography*, *45*, 259-271.
- 569 Hughes, G., & Griffiths, R. (2008). Horizontal convection. *Annual Review of Fluid*  
570 *Mechanics*, *40*, 185-208.
- 571 Ito, T., & Marshall, J. (2008, December). Control of lower-limb overturning circula-  
572 tion in the Southern Ocean by diapycnal mixing and mesoscale eddy transfer.  
573 *Journal of Physical Oceanography*, *38*, 2832 - 2845.
- 574 Johnson, G. C., & Bryden, H. L. (1989). On the size of the Antarctic Circumpolar  
575 Current. *Deep Sea Research*, *36*(1), 39-53.
- 576 Karsten, R., Jones, H., & Marshall, J. (2002). The role of eddy transfer in setting  
577 the stratification and transport of a circumpolar current. *Journal of Physical*  
578 *Oceanography*, *32*, 39-54.
- 579 Kuhlbrodt, T., Griesel, A., Montoya, M., Levermann, A., Hofmann, M., & Rahm-  
580 storf, S. (2007). On the driving processes of the Atlantic Meridional Overturn-  
581 ing Circulation. *Reviews of Geophysics*, *45*(2004RG000166), 1-32.
- 582 Kunnen, R. P. J., Stevens, R. J. A. M., Overkamp, J., Sun, C., van Heijst, G. F., &  
583 Clercx, H. J. H. (2011). The role of Stewartson and Ekman layers in turbu-  
584 lent rotating Rayleigh-Bénard convection. *Journal of Fluid Mechanics*, *688*,  
585 422-442.
- 586 Lumpkin, R., & Speer, K. (2007). Global ocean meridional overturning. *Journal of*  
587 *Physical Oceanography*, *37*, 2550-2562.
- 588 Marshall, D., Ambaum, M. H. P., Maddison, J. R., Munday, D. R., & Novak, L.  
589 (2017, January). Eddy saturation and frictional control of the antarctic cir-  
590 cumpolar current. *Geophysical Research Letters*, *44*, 286-292.
- 591 Marshall, J., & Radko, T. (2003, November). Residual-mean solutions for the  
592 Antarctic Circumpolar Current and its associated overturning circulation.  
593 *Journal of Physical Oceanography*, *33*, 2341-2354.
- 594 Marshall, J., & Speer, K. (2012, March). Closure of the meridional overturning cir-  
595 culation through Southern Ocean upwelling. *Nature Geoscience*, *5*, 171-180.
- 596 Meredith, M. P., & Hogg, A. M. (2006). Circumpolar response of Southern Ocean  
597 eddy activity to a change in the Southern Annular Mode. *Geophysical Research*  
598 *Letters*, *33*(L16608).
- 599 Morrison, A. K., Frolicher, T. L., & Sarmiento, J. L. (2015, January). Upwelling in  
600 the Southern Ocean. *Physics Today*, 27-32.
- 601 Morrison, A. K., & Hogg, A. M. (2013). On the relationship between Southern  
602 Ocean overturning and ACC transport. *Journal of Physical Oceanography*, *43*,  
603 140-148.
- 604 Munday, D. R., Johnson, H. L., & Marshall, D. P. (2013, March). Eddy satura-  
605 tion of equilibrated circumpolar currents. *Journal of Physical Oceanography*,  
606 *43*, 507-532.
- 607 Nikurashin, M., & Vallis, G. K. (2011, March). A theory of deep stratification and  
608 overturning circulation in the ocean. *Journal of Physical Oceanography*, *41*,  
609 485-502.
- 610 Nikurashin, M., & Vallis, G. K. (2012). A theory of the interhemispheric merid-  
611 ional overturning circulation and associated stratification. *Journal of Physical*

- 612 *Oceanography*, 42, 1652 - 1667.
- 613 Nurser, A. J. G., & Lee, M.-M. (2004, December). Isopycnal averaging at constant  
614 height. Part I: The formulation and a case study. *Journal of Physical Oceanog-*  
615 *raphy*, 34, 2721-2739.
- 616 Nycander, J., Nilsson, J., Döös, K., & Broström, G. (2007). Thermodynamic analy-  
617 sis of ocean circulation. *Journal of Physical Oceanography*, 37, 2038-2052.
- 618 Schmittner, A., & Weaver, A. J. (2001, March). Dependence of multiple climate  
619 states on ocean mixing parameters. *Geophysical Research Letters*, 28(6), 1027-  
620 1030.
- 621 Scotti, A., & White, B. (2011). Is horizontal convection really “non-turbulent?”.  
622 *Geophysical Research Letters*, 38, L21609.
- 623 Sohail, T., Gayen, B., & Hogg, A. M. (2018). Convection enhances mixing in the  
624 Southern Ocean. *Geophysical Research Letters*, 45, 1 - 10.
- 625 Stewart, A. L., & Thompson, A. F. (2013, July). Connecting Antarctic cross-slope  
626 exchange with Southern Ocean overturning. *Journal of Physical Oceanography*,  
627 43, 1453 - 1471.
- 628 Straub, D. N. (1993). On the transport and angular momentum balance of channel  
629 models of the Antarctic Circumpolar Current. *Journal of Physical Oceanogra-*  
630 *phy*, 23, 776-782.
- 631 Talley, L. D. (2013). Closure of the global overturning circulation through the In-  
632 dian, Pacific and Southern Oceans: Schematics and transports. *Oceanography*,  
633 26(1), 80-97.
- 634 Talley, L. D., Reid, J. L., & Robbins, P. E. (2003). Data-based meridional overturn-  
635 ing streamfunctions for the global ocean. *Journal of Climate*, 16, 3213-3226.
- 636 Toggweiler, J. R., Russell, J. L., & Carson, S. R. (2006). Midlatitude westerlies,  
637 atmospheric CO<sub>2</sub>, and climate change during the ice ages. *Paleoceanography*,  
638 21(PA2005).
- 639 Viebahn, J., & Eden, C. (2010). Towards the impact of eddies on the response of the  
640 Southern Ocean to climate change. *Ocean Modelling*, 34, 150-165.
- 641 Vreugdenhil, C. A., Gayen, B., & Griffiths, R. W. (2016). Mixing and dissipation  
642 in a geostrophic buoyancy-driven circulation. *Journal of Geophysical Research:*  
643 *Oceans*, 121, 6076-6091.
- 644 Ward, M. L., & Hogg, A. M. (2011). Establishment of momentum balance by form  
645 stress in a wind-driven channel. *Ocean Modelling*, 40, 133-146.
- 646 Wolfe, C. L., & Cessi, P. (2010). What sets the strength of the middepth stratifica-  
647 tion and overturning circulation in eddy ocean models? *Journal of Physical*  
648 *Oceanography*, 40, 1520 - 1538.
- 649 Wolfe, C. L., & Cessi, P. (2011). The adiabatic pole-to-pole overturning circulation.  
650 *Journal of Physical Oceanography*, 41, 1795 - 1810.
- 651 Zika, J. D., Sijp, W. P., & England, M. H. (2013, October). Vertical heat transport  
652 by ocean circulation and the role of mechanical and haline forcing. *Journal of*  
653 *Physical Oceanography*, 43, 2095 - 2112.
- 654 Zika, J. D., Sommer, J. L., Dufour, C. O., Molines, J.-M., Barnier, B., Brasseur,  
655 P., ... Vivier, F. (2013, May). Vertical eddy fluxes in the Southern Ocean.  
656 *Journal of Physical Oceanography*, 43, 941-955.



2018jc014883-f01-z-eps

